

Time-Reversal Symmetry Breaking in Re-Based Kagome Lattice Superconductor

Manasi Mandal,¹ A. Kataria,¹ P. K. Meena,¹ R. K. Kushwaha,¹ D. Singh,¹
P. K. Biswas,^{2,*} R. Stewart,² A. D. Hillier,² and R. P. Singh^{1,†}

¹*Department of Physics, Indian Institute of Science Education and Research Bhopal, Bhopal, 462066, India*

²*ISIS Facility, STFC Rutherford Appleton Laboratory, Didcot OX11 0QX, United Kingdom*

We investigated the Re-based kagome superconductor Re_2Zr through various measurements, including resistivity, magnetization, specific heat, and muon spin rotation and relaxation spectroscopy. These results suggest that Re_2Zr is a moderately coupled potential two-gap superconductor. Zero-field muon relaxation data indicate the possible presence of a time-reversal symmetry-breaking state in the superconducting ground state. Our investigation identifies Re_2Zr as a new unconventional superconductor with a potential complex order parameter that warrants considerable experimental and theoretical interest.

I. INTRODUCTION

Understanding unconventional superconductivity is a key focus in condensed matter physics, as the mechanism behind electron pairing remains unresolved. The crystal structure of a material significantly affects its electronic and superconducting properties. Recently, frustrated structures, such as kagome lattices, have attracted considerable attention due to their potential to host unconventional superconducting ground states [1–4]. Kagome lattice materials exhibit various exotic electronic features, including flat bands, Dirac cones, and non-trivial topological surface states, which have been both predicted [5, 6] and observed [7, 8]. The electronic correlations and intrinsic properties of the flat bands in kagome systems are believed to play a crucial role in the emergence of superconductivity, as demonstrated in the recently discovered AV_3Sb_5 compounds (where $\text{A} = \text{K}, \text{Cs}, \text{Rb}$) [1, 9, 10] and intermetallic “132” RT_3X_2 phases (where R is a rare earth metal, T is typically a 4d or 5d transition metal and X is $\text{B}, \text{Ga},$ or Si) [11–13]. Notably, in AV_3Sb_5 systems, superconductivity is accompanied by the breaking of translational, rotational, and time-reversal symmetries [8, 14].

Breathing kagome metal superconductors ROs_2 ($\text{R} = \text{Sc}, \text{Y}, \text{Lu}, \text{Zr}$ and Hf) have emerged as a promising platform for studying unconventional superconductivity. The kagome lattice formed by Os atoms in these compounds contributes to flat bands near the Fermi level, which are believed to play a role in their superconducting properties [15, 16]. In the isostructural compound Re_2Hf , a time-reversal symmetry-breaking pairing state has been observed [17], where the interplay between intra-band and inter-band Fermi surface nesting is thought to lead to unique superconducting ground states, with the superconducting gap changing sign across the nesting wavevector. Furthermore, the *ab initio* band structure calculations, corroborated by experimental evidence, have revealed a novel $s + is'$ state in Re_2Hf [17]. Given the

structural similarity between Re_2Hf and Re_2Zr , the latter compound presents an intriguing opportunity to explore unconventional superconductivity in kagome lattices. While Re_2Zr adopts a centrosymmetric C14 Laves phase, its underlying kagome net interleaved with triangular layers offers a unique platform for studying the interplay between kagome lattice geometry and superconducting properties.

Moreover, Re_2Zr can shed light on the unconventional superconducting ground state of Re-based compounds like Re_6X ($\text{X} = \text{Zr}, \text{Hf}$ and Ti). These compounds, with their non-centrosymmetric α -Mn structure, exhibit broken time-reversal symmetry (TRS), while Re-free compounds with similar structures preserve TRS [18–24]. This suggests that Re’s local electronic structure is crucial for understanding the unconventional superconducting states in the Re_6X series [25]. The variable Re/X ratio in Re-X binary compounds presents a unique opportunity to explore the relationship between Re and crystal structure in Re-based unconventional superconductors, making Re_2Zr a promising candidate for such studies.

This article presents a comprehensive study of the superconducting and normal-state properties of Re_2Zr . The crystal structure of Re_2Zr is composed of stacked kagome layers connected by intermediate 3D triangular layers, as illustrated in Fig. 1(a). The Re kagome layer consists of two non equilateral corner sharing triangles, forming a distorted kagome lattice distinct from the C15-type CaNi_2 structure [26]. This geometrical frustration can give rise to intriguing phenomena like flat bands and strong electronic correlations, potentially leading to unconventional superconducting ground states. Moreover, the high spin-orbit coupling of Re_2Zr could result in split electronic bands, further contributing to the formation of flat bands. The potential for these interesting features in Re_2Zr makes it a compelling subject for a detailed investigation of its superconducting properties.

II. EXPERIMENTAL DETAILS

A polycrystalline sample of Re_2Zr alloy was synthesized using the standard arc melting method. The phase purity of the sample was evaluated by powder X-ray

* Deceased

† rpsingh@iiserb.ac.in

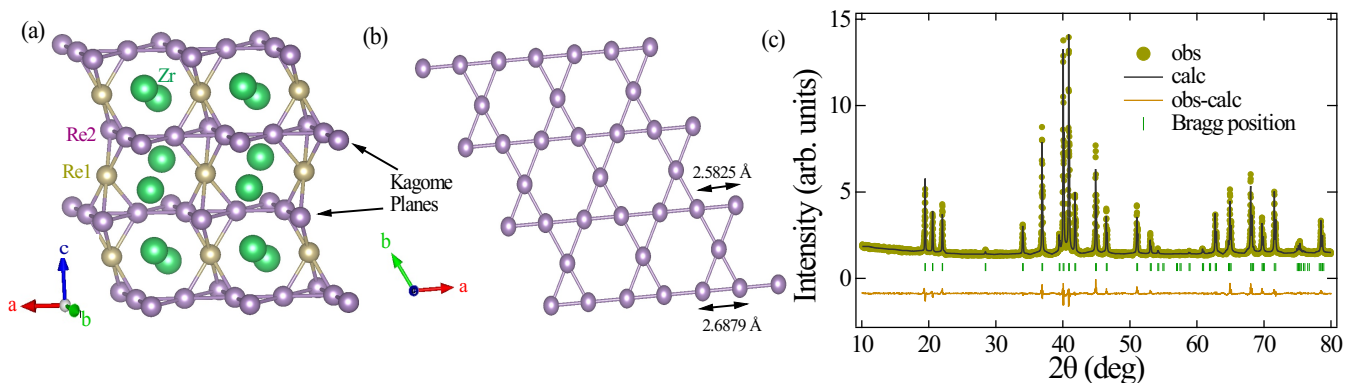


FIG. 1. (a) Crystal structure of Re_2Zr in the hexagonal MgZn_2 -type (C14) structure. (b) Distorted kagome layer in the ab -plane, showing Re2 atoms forming a network where two triangles and two hexagons meet at each vertex. (c) Rietveld refined powder XRD pattern, confirming crystallization in the space group $P6_3/mmc$.

diffraction (XRD) performed on a PANalytical X'pert Pro diffractometer, equipped with $\text{Cu } K\alpha$ radiation ($\lambda = 1.54056 \text{ \AA}$). Magnetization measurements were carried out using a Superconducting Quantum Interference Device (SQUID MPMS, Quantum Design). Specific heat and electrical resistivity measurements were conducted using a Physical Property Measurement System (PPMS, Quantum Design, Inc.). Muon spin rotation and relaxation (μSR) measurements were performed using the MuSR spectrometer at the ISIS pulsed muon source at the STFC Rutherford Appleton Laboratory, United Kingdom. These measurements utilize two batches of samples that possess identical properties and characteristics.

III. RESULTS AND DISCUSSION

a. Sample characterization

Re_2Zr crystallizes in a hexagonal MgZn_2 -type structure (C14 Laves phase), with the space group $P6_3/mmc$ (no. 194), as illustrated in Fig. 1(a) using the VESTA software [27]. Within each unit cell, two kagome layers are vertically stacked along the c direction at $z = 0.25$ and 0.75 , resulting in two non-equivalent Wyckoff sites for the Re1 and Re2 atoms. In this structure, the Re atoms form a trigonally distorted kagome lattice in the ab -plane, where each vertex is a convergence point for two triangles and two hexagons, as illustrated only for Re2 atoms in Fig. 1(b). The difference in the Re-Re bond lengths within the Re2 layer is ($d_{\text{Re2-Re2}}$) = 2.6879 and 2.5825 \AA with a slight variation for the Re1 layer. These bond lengths are comparable to those of other reported breathing kagome C14 Laves phase compounds [15, 16], suggesting a nearly ideal 2D kagome structure with minimal variation in bond lengths within the plane. The powder XRD pattern was refined using the Rietveld method implemented in FullProf Suite software [28], as shown in Fig. 1(c). The refined lattice parameters are $a = b = 5.270(5) \text{ \AA}$, and $c = 8.636(2) \text{ \AA}$, with $V_{\text{cell}} =$

207.782(4) \AA^3 , which are consistent with values previously reported in the literature [29].

b. Electrical resistivity

The temperature dependence of the electrical resistivity $\rho(T)$ in zero applied magnetic field is shown in Fig. 2(a). Resistivity decreases with decreasing temperature and reaches zero at 6.65(3) K, indicating the superconducting phase transition. Additionally, magnetization measurements (inset of Fig. 2(a)) reveal the presence of a superconducting state at $T_C^{\text{onset}} = 6.65(3) \text{ K}$ (onset of a strong diamagnetic signal) with an approximate superconducting fraction of $\sim 100\%$. The residual resistivity ratio was estimated to be $\rho(300 \text{ K})/\rho(10 \text{ K}) = 8.86$. In the high-temperature region up to 300 K, the metallic nature of $\rho(T)$ fit well with the parallel resistor model [31]. According to this model, the evolution of ρ with temperature can be understood by the following expression:

$$\frac{1}{\rho(T)} = \frac{1}{\rho_1(T)} + \frac{1}{\rho_{\text{sat}}} \quad (1)$$

where ρ_{sat} is the saturation resistivity, and $\rho_1(T)$ is the temperature-dependent resistivity. Furthermore, $\rho_1(T)$ is given by the following expression:

$$\rho_1(T) = \rho_0 + r \left(\frac{T}{\theta_R} \right)^5 \int_0^{\theta_R/T} \frac{x^5}{(e^x - 1)(1 - e^{-x})} dx \quad (2)$$

where ρ_0 is the residual resistivity, θ_R is the Debye temperature, and r is a material-dependent pre-factor. This term is the Bloch-Grüneisen term accounting for phonon-assisted electron scattering similar to s-d scattering in transition metal compounds [32]. Fitting the experimental data with this model yields $\rho_{\text{sat}} = 265(3) \mu\Omega \text{ cm}$, $\theta_R = 250(3) \text{ K}$, and $\rho_0 = 13.7(2) \mu\Omega \text{ cm}$. This value of θ_R is close to the value obtained from the heat capacity data (described later), suggesting that the parallel resistor model can successfully explain the temperature dependence of $\rho(T)$ above the superconducting region.

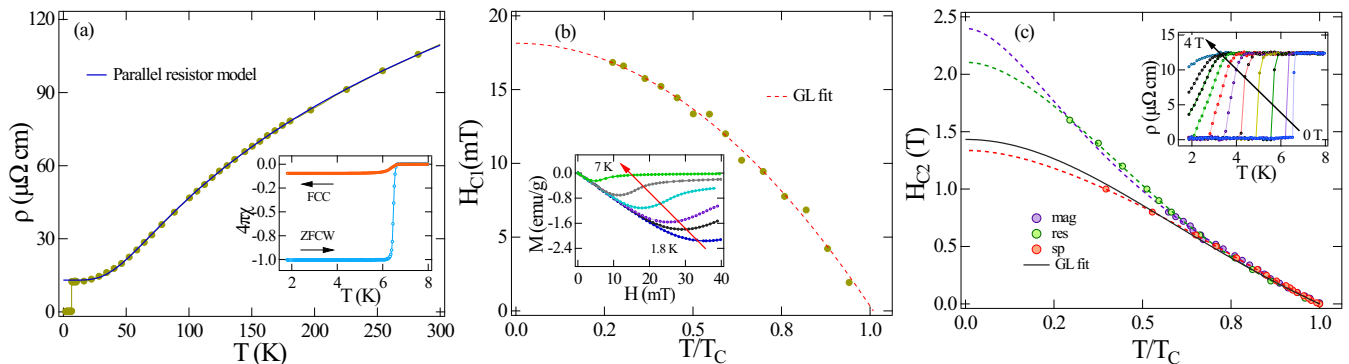


FIG. 2. (a) Temperature dependence of the resistivity in zero field. The inset displays magnetization data in ZFCW and FCC mode in a field of 1.0 mT. (b) Temperature dependence of the lower critical field H_{C1} , which was fitted using the Ginzburg-Landau relation. The inset shows low-field magnetization curves at different temperatures. (c) The zero-temperature upper critical field, $H_{C2}(0)$, was determined from magnetization, resistivity, and specific heat measurements (violet circles, green circles, and orange circles, respectively). The solid black line represents the Ginzburg-Landau fit, while the two-gap fittings[30] are indicated by the dotted lines. The variation of $\rho(T)$ under various applied magnetic fields is shown in the inset.

c. Magnetization

The lower critical field, $H_{C1}(T)$, was extracted from the low-field magnetization curves $M(H)$, as shown in the inset of Fig. 2(b). $H_{C1}(0)$ was estimated to be 18.4(1) mT by fitting the data using the Ginzburg-Landau (GL) equation $H_{C1}(T) = H_{C1}(0) \left[1 - \left(\frac{T}{T_C} \right)^2 \right]$, as shown in Fig. 2(b). The upper critical field, $H_{C2}(T)$, was determined from magnetization, resistivity, and specific heat measurements. The inset of Fig. 2(c) shows the temperature dependence of ρ in the vicinity of T_C under various applied magnetic fields. As the applied field increased, T_C shifted to a lower value, as expected for a superconductor. In the high-field and low-temperature region, the data deviate from the GL relation $H_{C2}(T) = H_{C2}(0) \frac{(1-t^2)}{(1+t^2)}$, where $t = T/T_C$ (Fig. 2(c)). The data were well fitted with the two-gap model [17, 30], as indicated by the dotted lines in Fig. 2(c). From the magnetization data, the estimated value of $H_{C2}^{mag}(0)$ is 2.39(1) T. The Pauli limiting field within the BCS theory is given by $H_{C2}^p(0) = 1.83 T_C$, which gives $H_{C2}^p(0) = 12.0(1)$ T.

The Ginzburg-Landau coherence length $\xi_{GL}(0)$ was calculated to be 117(2) Å using the relation $H_{C2}(0) = \frac{\Phi_0}{2\pi\xi_{GL}^2}$, where Φ_0 is the magnetic flux quantum ($= 2.07 \times 10^{-15}$ T m²) [33]. The GL penetration depth, $\lambda_{GL}(0)$, was subsequently determined to be 1515(3) Å, using the relations Eq.(3),

$$H_{C1}(0) = \left(\frac{\Phi_0}{4\pi\lambda_{GL}^2(0)} \right) \ln \left(\frac{\lambda_{GL}(0)}{\xi_{GL}(0)} + 0.497 \right). \quad (3)$$

The GL parameter $k_{GL} = \frac{\lambda_{GL}(0)}{\xi_{GL}(0)}$ was found to be 12.9(2), which is much higher than $\frac{1}{\sqrt{2}}$, and classifies Re_2Zr as a type-II superconductor. The thermodynamic critical field, H_C , is related to the lower and upper critical fields by the relation $H_{C1}(0)H_{C2}(0) = H_C^2 \ln k_{GL}$, with a calculated value of H_C around 0.13(2) T.

d. Specific heat

Temperature-dependent specific heat measurements, $C(T)$, were performed to analyze the superconducting state of the sample. The zero field $C(T)/T$ as a function of T^2 is shown in Fig. 3(a), while the magnetic field dependence is presented in Fig. 3(b) over the range of 0-1 T. A pronounced jump in the specific heat data at 6.46(2) K confirms bulk superconductivity. The low-temperature normal-state specific heat data were fitted using the relation,

$$\frac{C}{T} = \gamma_n + \beta_3 T^2 + \beta_5 T^4 \quad (4)$$

where γ_n is the Sommerfeld coefficient, β_3 is the Debye constant, and β_5 is the anharmonic contribution to the specific heat. We obtain the fitting parameters as $\gamma_n = 12.9(4)$ mJ mol⁻¹ K⁻², $\beta_3 = 0.22(1)$ mJ mol⁻¹ K⁻⁴ and $\beta_5 = 1.1(7) \times 10^{-4}$ μJ mol⁻¹ K⁻⁶. From the experimental value of β_3 , the Debye temperature θ_D of the compound can be calculated using the simple Debye model for the phonon contribution to the specific heat in Eq. (5):

$$\theta_D = \left(\frac{12\pi^4 RN}{5\beta_3} \right)^{\frac{1}{3}}, \quad (5)$$

where N ($= 3$) is the number of atoms per formula unit and R is the molar gas constant ($= 8.314$ J mol⁻¹ K⁻¹). The estimated value of θ_D is 297(5) K. For non-interacting particles, γ_n is proportional to the density of states $D_C(E_F)$ at the Fermi level, which is calculated to be $5.47 \frac{\text{states}}{eVf.u.}$ from the relation $\gamma_n = \left(\frac{\pi^2 k_B^2}{3} \right) D_C(E_F)$, where $k_B \simeq 1.38 \times 10^{-23}$ J K⁻¹. The electron-phonon coupling constant λ_{e-ph} is estimated as 0.70(1) using the McMillan theory [34], stated as:

$$\lambda_{e-ph} = \frac{1.04 + \mu^* \ln(\theta_D/1.45T_C)}{(1 - 0.62\mu^*) \ln(\theta_D/1.45T_C) - 1.04}, \quad (6)$$

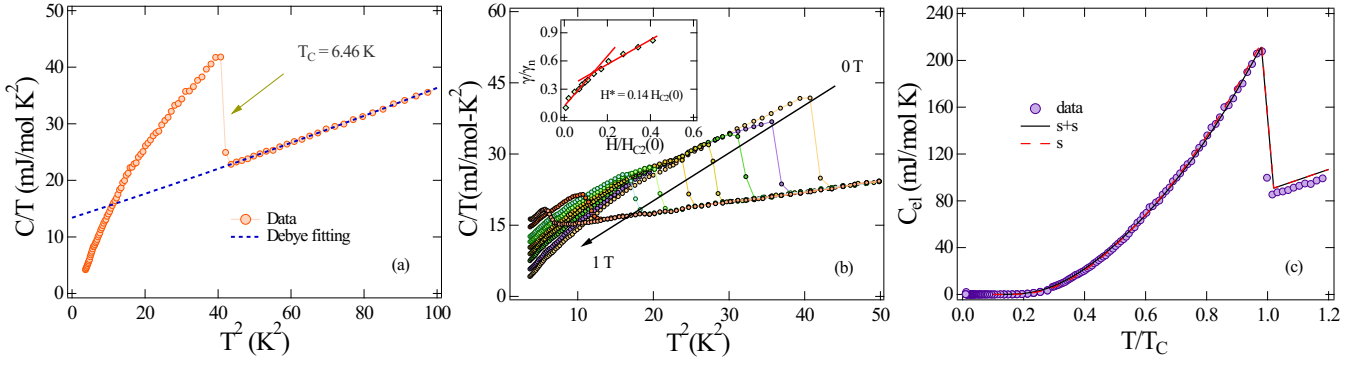


FIG. 3. Specific heat divided by temperature, $C(T)/T$, plotted against T^2 in (a) zero field fitted with the Debye model and (b) as a function of applied magnetic field. The variation of the Sommerfeld coefficient γ with respect to the magnetic field is depicted in the inset. (c) The temperature dependence of C_{el} fitted using the s (red dotted line) and $s + s$ models (black line) using Eq.(11).

where μ^* ($= 0.13$ for many intermetallic superconductors) is the repulsive screened Coulomb parameter. This value of λ_{e-ph} suggests that Re_2Zr is a moderately coupled superconductor similar to Re_2Hf [17], Zr_2Ir [35] and other A15 compounds such as Ti_3Ir [36] and Ti_3Sb [36].

The electronic contribution to the specific heat in the superconducting state $C_{el}(T)$ can be calculated by subtracting the phononic contribution from the measured data $C(T)$ using the equation $C_{el}(T) = C(T) - \beta_3 T^3 - \beta_5 T^5$. The magnitude of the specific heat jump $\frac{\Delta C_{el}}{T_C}$ at T_C is $19.33 \text{ mJ mol}^{-1} \text{ K}^{-2}$. This gives a normalized specific heat jump of $\frac{\Delta C_{el}}{\gamma_n T_C} = 1.50(5)$, which is slightly higher than the BCS value (1.43) in the weak coupling limit. In the superconducting state, the Sommerfeld coefficient γ was calculated by fitting C_{el}/T versus T with equation $\frac{C_{el}}{T} = \gamma + \frac{A}{T} \exp\left(\frac{-bT}{T_C}\right)$, with A and b being the fitting parameters [37]. The field dependence of γ is shown in the inset of Fig. 3(b), where γ and H are normalized by γ_n and $H_{C2}(0)$. Here we observe that in the lower field region γ increases linearly as a function of H up to the crossover field $H^* = 0.14 \times H_{C2}(0)$, which is slightly less than the proposed theoretical value of $0.3 \times H_{C2}(0)$ for a completely isotropic gap superconductor [38, 39]. Similar behaviour has been observed in Re_2Hf [17]. The field dependence observed in γ suggests the possibility of an unconventional superconducting energy gap. To find the nature of the energy gap, the electronic contribution to the specific heat data at zero field in the superconducting region was fitted using the α -model [40] as follows:

$$\frac{C_{el}}{\gamma_n T_C} = t \frac{d(S/\gamma_n T_C)}{dt}, \quad (7)$$

$$\frac{S}{\gamma_n T_C}(t) = -\frac{3}{\pi^3} \int_0^{2\pi} \int_0^\infty [f \ln f + (1-f) \ln(1-f)] d\epsilon d\theta, \quad (8)$$

$$f = \left[\exp\left(\frac{(\epsilon^2 + A^2(t, \theta)/4)^{0.5}}{t}\right) + 1 \right]^{-1}, \quad (9)$$

and

$$\delta(T) = \frac{\Delta(T)}{\Delta(0)} = \tanh \left[1.82 \left(1.018 \left(\frac{T_C}{T} - 1 \right) \right)^{0.51} \right], \quad (10)$$

where $t = \frac{T}{T_C}$, $A(t, \theta) = \alpha g_k(\theta) \delta(T)$, and $\alpha = 2 \frac{\Delta(0)}{k_B T_C}$. $g_k(\theta)$ is the azimuthal angle-dependent part of the energy, which is different for different gap functions and depends on the gap symmetry. For an isotropic s gap, g_k is taken as 1. In the case of the two-band phenomenological α -model, the contributions of each band can be calculated within the above model with corresponding weight factors ω and $(1 - \omega)$ as follows:

$$C(T) = \omega C_1(T) + (1 - \omega) C_2(T) \quad (11)$$

The best fit to the data was obtained with the $s + s$ model compared to the s model, as shown in Fig. 3(c). The gap values obtained by fitting C_{el} with a two-gap model are 1.9 and 1.4, with a weight factor (see the fraction of the gap, ω) of 0.68 (goodness of fit, $\chi^2 = 1.21$). In comparison, the gap value for a single s -wave model is $\frac{\Delta(0)}{k_B T_C} = 1.7$ ($\chi^2 = 1.35$). To find the exact superconducting gap structure, local probe measurements, e.g., muon spin rotation and relaxation measurements, are vital.

e. Muon Spin Rotation and Relaxation

Transverse field (TF) μSR measurements were performed in the vortex state to investigate the superconducting gap structure. Measurements were performed after the sample was field-cooled, where a field $H = 30 \text{ mT}$ ($H_{C1} < H < H_{C2}$) was applied perpendicular to the initial muon spin polarization. The TF- μSR spectra collected above and below T_C are shown in Fig. 4(a). The normal state ($T = 8.0 \text{ K}$) shows oscillatory spectra suggesting a homogeneous field distribution throughout the sample, with weak depolarization arising from the dipolar nuclear field. In contrast, the asymmetry spectra in the superconducting state ($T = 0.4 \text{ K}$) show

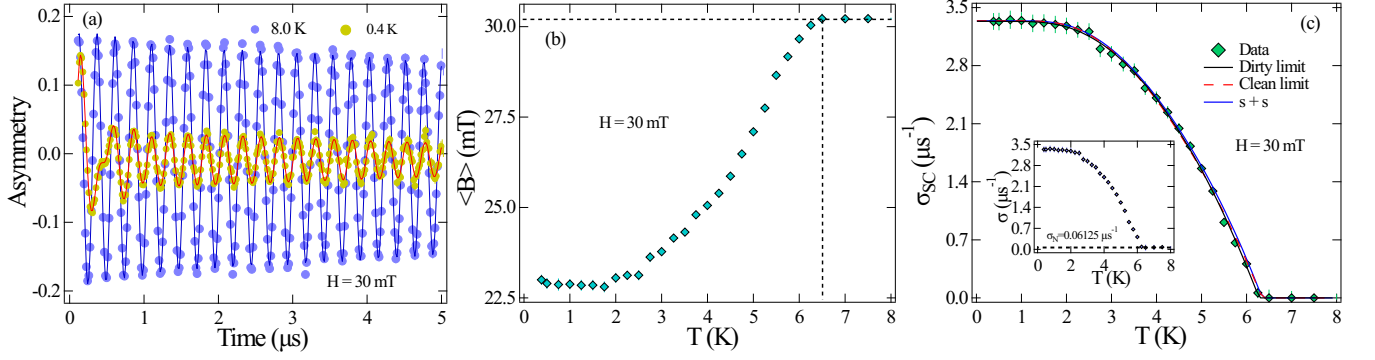


FIG. 4. (a) TF- μ SR asymmetry spectra measured above ($T = 8.0$ K) and below ($T = 0.4$ K) the T_C in an applied field $H = 30$ mT, where solid lines represent fits the data using Eq. 12. (b) Temperature variation of the internal magnetic field (B). (c) Temperature dependence of the depolarization rate σ_{sc} is fitted using a dirty and clean limit s -wave model, represented by the black solid line and red dotted line, respectively, along with the $s + s$ model (blue solid line). Inset shows the temperature dependence of the effective depolarization rate σ .

strong depolarization, indicating an inhomogeneous field distribution resulting from the flux line lattice state. The time-domain spectra were best fitted using a multicomponent Gaussian damped oscillatory function with an undamped oscillatory background term that emerges from the muons implanted directly into the silver sample holder that does not depolarize, represented as:

$$G_{TF}(t) = \sum_{i=1}^N A_i \exp\left(\frac{-\sigma_i^2 t^2}{2}\right) \cos(\gamma_\mu B_i t + \phi) + A_{bg} \cos(\gamma_\mu B_{bg} t + \phi) \quad (12)$$

where ϕ is the phase of the initial muon spin polarization with respect to the positron detector. A_i and B_i , are the asymmetry and mean field (first moment) of the i^{th} component of the Gaussian distribution, respectively. σ_i is the depolarization/relaxation rate and $\gamma_\mu/2\pi = 135.5$ MHz/T is the muon gyromagnetic ratio. A_{bg} and B_{bg} are the background contributions for the asymmetry and the field, respectively. The temperature dependence of the effective depolarization rate σ was calculated using the second-moment method [41]. Here, the first and second moments are described as Eq.(13) and Eq.(14):

$$\langle B \rangle = \sum_{i=1}^N \frac{A_i B_i}{A_1 + A_2 + \dots + A_N} \quad (13)$$

$$\langle \Delta B^2 \rangle = \sum_{i=1}^N \frac{A_i [(\sigma_i/\gamma_\mu)^2 + (B_i - \langle B \rangle)^2]}{A_1 + A_2 + \dots + A_N} = \frac{\sigma^2}{\gamma_\mu^2}. \quad (14)$$

The asymmetry spectra (Fig. 4(a)) were fitted with three Gaussian components. The temperature variation of the internal magnetic field, $\langle B \rangle$, is depicted in Fig. 4(b), while the temperature dependence of the effective depolarization rate σ , as extracted using Equations (12-14), is shown in the inset of Fig. 4(c). σ incorporates depolarization arising from the nuclear dipole moments (σ_N) and the field variation across the flux line

lattice (σ_{sc}), as expressed by the quadratic relation: $\sigma^2 = \sigma_{sc}^2 + \sigma_N^2$, which we used to extract σ_{sc} from the data.

The temperature dependence of σ_{sc} (Fig. 4(c)) is seen to be nearly constant below $\simeq T_C/3$, indicating the absence of nodes in the superconducting energy gap at the Fermi surface. This nature can be well described by the s -wave model in the dirty limit as given by;

$$\frac{\sigma_{sc}(T)}{\sigma_{sc}(0)} = \frac{\lambda^{-2}(T)}{\lambda^{-2}(0)} = \frac{\Delta_0(T)}{\Delta_0(0)} \tanh\left[\frac{\Delta_0(T)}{2k_B T}\right] \quad (15)$$

$\Delta_0(T)/\Delta_0(0) = \tanh\{1.82(1.018(T_C/T - 1))^{0.51}\}$ is the BCS approximation for temperature-dependent energy gap and $\Delta_0(0)$ is the gap value at zero temperature. We have also fitted the data within the semiclassical approximation of the clean limit using Eq.(16):

$$\frac{\sigma_{sc}^{-2}(T, \Delta_0)}{\sigma_{sc}^{-2}(0, \Delta_0)} = 1 + \frac{1}{\pi} \int_0^{2\pi} \int_{\Delta_k(T, \phi)}^{\infty} \left(\frac{\delta f}{\delta E}\right) \frac{E dE d\phi}{\sqrt{E^2 - \Delta_k^2(T, \phi)}}, \quad (16)$$

where $f = [1 + \exp(E/k_B T)]^{-1}$ is the Fermi function and $\Delta_k(T, \phi) = \Delta_0(T) g_k(\phi)$. $\Delta_0(T)$ is the value of the BCS gap and g_k is the angular dependence of the gap, which depends on the gap symmetries [42]. Moreover, for the two-gap model, the temperature dependence of σ_{sc}^{-2} can be expressed as the linear combination of two components, Eq.(17):

$$\frac{\sigma_{sc}^{-2}(T)}{\sigma_{sc}^{-2}(0)} = \omega \frac{\sigma_{sc}^{-2}(T, \Delta_{0,1})}{\sigma_{sc}^{-2}(0, \Delta_{0,1})} + (1 - \omega) \frac{\sigma_{sc}^{-2}(T, \Delta_{0,2})}{\sigma_{sc}^{-2}(0, \Delta_{0,2})}, \quad (17)$$

where $\Delta_{0,1}$ and $\Delta_{0,2}$ are the gap waves with the weight factor ω and $(1 - \omega)$. We have obtained a good fit for the data using the s -wave dirty limit model, providing a gap value of $\frac{\Delta_0(0)}{k_B T_C} = 1.65(1)$ ($\chi^2 = 1.12$). The μ SR data fitted with the $s + s$ model yield gap values of 2.35 and 1.83, with a weight factor of 0.25 ($\chi^2 = 1.30$), while for the single s -wave clean-limit fit, the gap value is $\frac{\Delta_0(0)}{k_B T_C} = 1.90$ ($\chi^2 = 1.24$). The different model fittings for the temperature dependence of σ_{sc} are shown in Fig. 4(c).

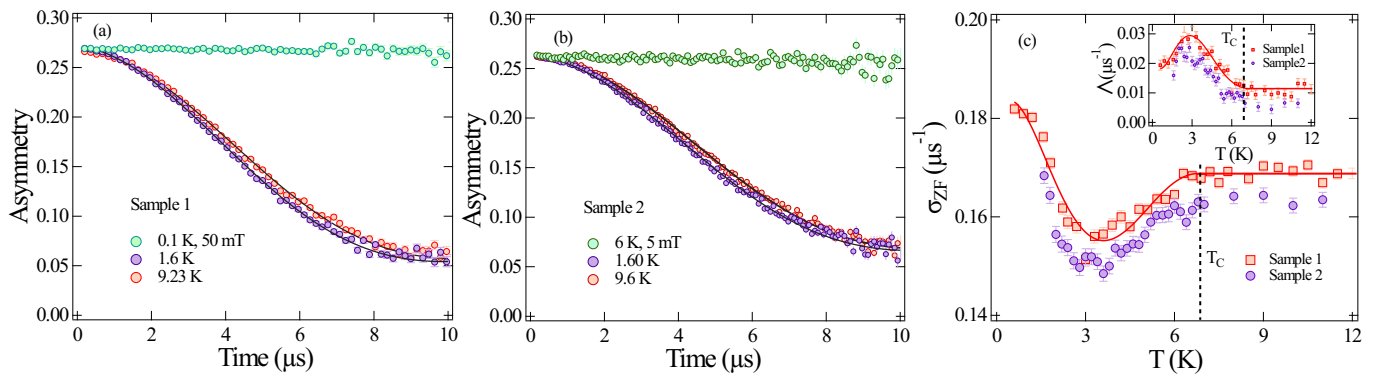


FIG. 5. (a) and (b) Time evolution of the spin polarization of muons above and below T_C under zero-field conditions for two batches of sample. The solid lines show the fitting of the asymmetry spectra using Eq. 19 and 20. (c) Temperature dependence of relaxation rate σ_{ZF} . The inset shows the temperature dependence of relaxation rate Λ . Here, the solid red line represents a guide-to-the-eye for the change in relaxation rates.

In a type-II isotropic superconductor with a hexagonal Abrikosov vortex lattice having $\kappa > 5$, the penetration depth λ can be calculated with a high degree of accuracy, using Eq. (18) [43, 44],

$$\sigma_{sc}[\mu s^{-1}] = 4.854 \times 10^4 (1-h) [1 + 1.21(1-\sqrt{h})^3] \lambda^{-2} [nm^{-2}], \quad (18)$$

where $h = H/H_{C2}(T)$ is the reduced field. Using the measured H_{C2} (T), λ was determined to be 1628(2) Å.

The asymmetry spectra in zero field (ZF), measured above and below the superconducting transition temperature, are shown in Fig. 5(a) and (b) for two batches of samples labeled 1 and 2. Both batches were synthesized using the same preparation method and displayed similar superconducting characteristics based on magnetization and specific heat measurements. A slight change in relaxation behavior is observed in the superconducting state compared to the normal state for both batches. Furthermore, a low longitudinal field of 50 mT in the superconducting state (0.1 K) fully decouples the muon spins from relaxation, as shown in Fig. 5 (a), while a similar decoupling effect is observed for batch 2 at 6 K and 5 mT. This suggests that the magnetic field in the superconducting state is quasi-static for both batches. To better understand this behavior, ZF- μ SR data were fitted using a damped Gaussian Kubo-Toyabe function [45] with a background contribution associated with muons stopping in the silver sample holder. The asymmetry fitting function is given by:

$$G(t) = A_1 \exp(-\Lambda t) G_{KT}(t) + A_{bg}, \quad (19)$$

with

$$G_{KT}(t) = \frac{1}{3} + \frac{2}{3} (1 - \sigma_{ZF}^2 t^2) \exp\left(\frac{-\sigma_{ZF}^2 t^2}{2}\right), \quad (20)$$

where A_1 is the initial sample asymmetry, and σ_{ZF} and Λ are the Gaussian and an additional relaxation rate, respectively. All parameters were allowed to vary freely during the fitting of the asymmetry spectra, and the temperature dependence of the relaxation rates for the two

samples is shown in Fig. 5(c). The background and sample asymmetry, A_{bg} and A_1 are almost temperature independent with no observable trend, while relaxation rates σ_{ZF} and Λ show a significant change in the superconducting state. Above T_C (marked by a vertical dashed black line), both relaxation parameters σ_{ZF} and Λ are temperature independent. In the superconducting state, as the temperature decreases, σ_{ZF} initially decreases until it reaches a temperature $T' \simeq 3.1$ K, where it starts to increase again but does not saturate to the lowest measured temperature, creating a valley-like behavior at T' , a temperature significantly different from T_C . In contrast, Λ exhibits a peak-like behaviour at the same temperature T' . The increase in relaxation σ_{sc} below T' can be associated with the presence of a spontaneous magnetic field, indicating the break of the time-reversal symmetry in the superconducting state. For sample 1, the calculated spontaneous field $B_{int} = 0.22$ G is comparable to that observed in other time-reversal symmetry-broken superconductors, providing strong evidence for a broken TRS pairing state [17, 25, 46, 47].

We explored various approaches to understand this phenomenon. One possibility is that the two relaxation rates, σ_{ZF} and Λ , may be interdependent, causing one to exhibit a valley and the other a peak. To test this hypothesis, we performed fits while keeping Λ fixed. A similar valley trend with significant change is observed in σ_{ZF} ; however, this approach resulted in a poor fit of the asymmetry spectra. We further attempted to fit the spectra using various fitting functions, including the stretched and Lorentzian-damped Gaussian Kubo-Toyabe functions. However, a valley trend in the relaxation parameters persisted. Notably, this behavior was consistently observed in both sample sets, 1 and 2, measured in different sample environments and a year apart, underscoring its intrinsic nature and independence from external parameters. Additionally, changes in both the channels of the muon relaxation are not new and have previously been observed in several TRS broken systems such as La_7Ir_3 , La_7Pd_3 , La_7Rh_3 [48–50] and $\text{Pr}_{1-x}\text{La}_x\text{Pt}_4\text{Ge}_{12}$, $\text{Pr}(\text{Os}_{1-x}\text{Ru}_x)_4\text{Sb}_{12}$, $\text{Pr}_{1-y}\text{La}_y\text{Os}_4\text{Sb}_{12}$ [51, 52] and

$\text{Lu}_3\text{Os}_4\text{Ge}_{13}$ [53]. In these cases, the increase in the secondary relaxation channel is attributed to nuclear spin fluctuations, which may also be the cause of the observed increase starting at T' . In particular, our magnetization, specific heat, and resistivity measurements, along with TF- μ SR results, do not exhibit any anomaly at T' , and longitudinal field μ SR measurements also rule out the presence of any external magnetic field impurity. The valley/dip in the relaxation rate is observed in many other TRS broken superconductors $\text{PrPt}_4\text{Ge}_{12}$ [46], $\text{Pr}_{1-x}\text{Ce}_x\text{Pt}_4\text{Ge}_{12}$ [54], $\text{Pr}_{1-x}\text{La}_x\text{Pt}_4\text{Ge}_{12}$ [52] and recently in La_7Ni_3 [55] and $\text{Lu}_3\text{Os}_4\text{Ge}_{13}$ [53]. These results suggest the possibility of multicomponent order parameters with a multi-gap superconducting state.

It is also worth noting that while this trend has been observed in some potential multicomponent, multigap superconductors, it is not specific to any crystal symmetry or spin-orbit coupling (SOC) strength. For example, La_7Ni_3 shows a dip feature, whereas La_7Ir_3 , La_7Pd_3 , and La_7Rh_3 do not, where La_7Ni_3 has lower SOC compared to others [48–50, 55]. Similarly, $\text{Lu}_3\text{Os}_4\text{Ge}_{13}$ with high SOC exhibits a dip feature in the relaxation, whereas $\text{Y}_3\text{Ru}_4\text{Ge}_{13}$ does not [53, 56]. In our case, the dip/valley-like trend is noted in Re_2Zr but not in Re_2Hf [17], suggesting that the underlying mechanism may be complex and potentially related to the interplay of multiple superconducting gaps within the material.

Theoretical studies on Re_2Hf have suggested that geometric frustration-driven spin-fluctuations could mediate unconventional superconducting pairing. Given the similarity between Re_2Zr and Re_2Hf , and the evidence of spin-fluctuations in Re_2Zr from μ SR measurements, it is plausible that this mechanism might also be at play in Re_2Zr [17]. While Re_2Zr and Re_2Hf differ in their spin-orbit coupling due to the 4d/5d elements, the presence of geometric frustration within the kagome layer appears to be a crucial factor in establishing an unconventional superconducting ground state in both compounds. Moreover, the Re element itself might be responsible for the unconventional superconducting ground state [25]. However, the complex unit cell structure of these compounds [15, 16], comprising two kagome layers and a triangular layer, makes it challenging to definitively pinpoint the pairing mechanism. To achieve a conclusive understanding, further investigations involving single-crystal experiments and in-depth band structure calculations are necessary.

Uemura et al. [59–62] have described a method for classifying superconductors based on the ratio of the critical temperature T_C to the effective Fermi temperature T_F . In this classification, exotic superconductors fall in the range $0.01 \leq \frac{T_C}{T_F} \leq 0.1$, whereas conventional BCS superconductors have $\frac{T_C}{T_F} \leq 0.001$. We calculated T_F using the relation $k_B T_F = \frac{\hbar^2}{2} (3\pi^2)^{2/3} \frac{n_s^{2/3}}{m^*}$ [63]. Here, we estimate the superconducting carrier density n_s by $n_s(0) = \frac{m^*}{\mu_0 e^2 \lambda^2}$, where $m^* = (1 + \lambda_{e-ph})m_e$. Using $\lambda = 1628 \text{ \AA}$ (from muon spectroscopy measurements) and $\lambda_{e-ph} = 0.70$ (from specific heat data), we estimated

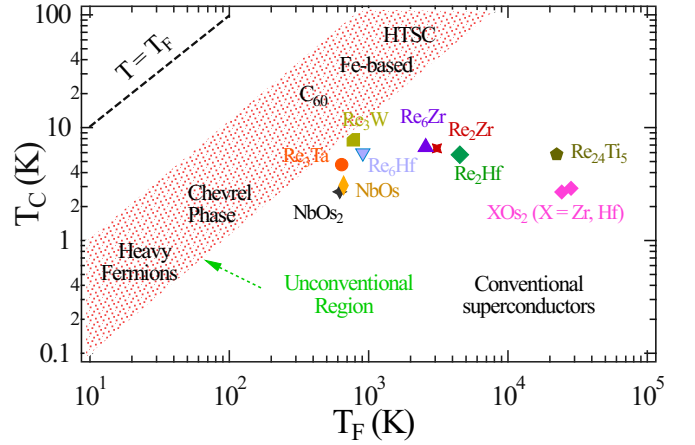


FIG. 6. Uemura plot of Re_2Zr along with Re_2Hf [17] and Re_6X [18, 57, 58], and other unconventional materials represented by the red band.

TABLE I. Normal and superconducting parameters of Re_2Zr in comparison with Re_2Hf [17] and Re_6Zr [18].

Parameters	unit	Re_2Zr	Re_2Hf	Re_6Zr
T_C	K	6.6(2)	5.7(2)	6.75
ρ_0	$\mu\Omega\text{cm}$	13.7(2)	22.0(1)	142
$H_{C1}(0)$	mT	18.4(2)	12.7(2)	10.3
$H_{C2}(0)$	T	2.39(1)	1.17(2)	11.2
$H_{C2}^P(0)$	T	12.0(1)	10.5	12.35
ξ_{GL}	\AA	117(2)	168	53.7
λ_{GL}	\AA	1515(3)	1739	2470
k_{GL}		12.9(2)	10.36(1)	46.2
γ_n	mJ/mol K ²	12.9(4)	11.04(2)	26.9
θ_D	K	297(5)	293.8	338
$\frac{\Delta C_{eL}}{\gamma_n T_C}$		1.50(5)	1.41	1.60
λ_{e-ph}		0.70(1)	0.67	0.67
$D_C(E_F)$	states/eV f.u.	5.47	4.69	
n	10^{26}m^{-3}	18.0	24.8	15.2
$\frac{m^*}{m_e}$		1.70	7.8	10.1
T_F	K	3091(6)	4514	2570
$\frac{T_C}{T_F}$		0.0021(1)	0.0013	0.0026

$T_F = 3091(6) \text{ K}$, resulting in a corresponding value of $\frac{T_C}{T_F} = 0.0021(1)$ for Re_2Zr . This ratio places the compound Re_2Zr outside the band of unconventional families but close to the broken TRS superconductors Re_2Hf [17] and Re_6X [18, 57, 58]. The Uemura plot of Re_2Zr , along with Re_2Hf and some other unconventional materials [23, 24, 64–67], is shown in Fig. 6. A summary of all experimentally measured and estimated parameters, compared with those for Re_2Hf and Re_6Zr , is provided in Table I.

IV. CONCLUSION

In summary, we have investigated the Re-based kagome lattice superconductor Re_2Zr through transport, magnetization, specific heat, and muon-spin rotation and relaxation measurements. Our findings unequivocally establish Re_2Zr as a type-II superconductor with moderately coupled Cooper pairs. The upward curvature observed in the upper critical field and the specific heat data suggest that Re_2Zr may exhibit characteristics of a two-nodeless gap superconductor akin to the behavior observed in the Re_2Hf alloy. Furthermore, the non-linear response of γ at low fields hints at the presence of an unconventional superconducting energy gap. The transverse field muon-spin rotation (TF- μSR) data further confirm the existence of two-gap superconductivity.

Furthermore, zero-field and longitudinal-field μSR data suggest time-reversal symmetry breaking in the superconducting ground state and suggest a potential unconventional pairing mechanism, which underlies the superconductivity in Re_2Zr . This comprehensive investigation underscores the need for further exploration, particularly on Re_2Zr single crystals, to elucidate potential complex-order parameters similar to those observed in Re_2Hf . This work will be valuable for understanding the complex superconducting ground state of kagome-structured superconductors, where the pairing mechanism remains elusive.

V. ACKNOWLEDGMENTS

R.P.S. acknowledges the SERB Government of India for the Core Research Grant No. CRG/2023/000817.

-
- [1] Y.-X. Jiang, J.-X. Yin, M. M. Denner, N. Shumiya, B. R. Ortiz, G. X. Z. Guguchia, J. He, M. S. Hossain, X. Liu, J. Ruff, L. Kautzsch, S. S. Zhang, G. Chang, I. Belopolski, Q. Zhang, T. A. Cochran, D. Multer, M. Litskevich, Z.-J. Cheng, X. P. Yang, Z. Wang, R. Thomale, T. Neupert, S. D. Wilson, and M. Z. Hasan, *Nat. Mater.* **20**, 1353 (2021).
- [2] B. R. Ortiz, P. M. Sarte, E. M. Kenney, M. J. Graf, S. M. L. Teicher, R. Seshadri, and S. D. Wilson, *Phys. Rev. Mater.* **5**, 034801 (2021).
- [3] F. H. Yu, T. Wu, Z. Y. Wang, B. Lei, W. Z. Zhuo, J. J. Ying, and X. H. Chen, *Phys. Rev. B* **104**, L041103 (2021).
- [4] T. Neupert, M. M. Denner, J.-X. Yin, R. Thomale, and M. Z. Hasan, *Nat. Phys.* **18**, 137 (2022).
- [5] A. Bolens and N. Nagaosa, *Phys. Rev. B* **99**, 16 (2019).
- [6] S. Peng, Y. Han, G. Pokharel, J. Shen, Z. Li, M. Hashimoto, D. Lu, B. R. Ortiz, Y. Luo, H. Li, M. Guo, B. Wang, S. Cui, Z. Sun, Z. Qiao, S. D. Wilson, and J. He, *Phys. Rev. Lett.* **127**, 266401 (2021).
- [7] J.-X. Yin, B. Lian, and M. Z. Hasan, *Nature* **612**, 647 (2022).
- [8] K. Jiang, T. Wu, J.-X. Yin, Z. Wang, M. Z. Hasan, S. D. Wilson, X. Chen, and J. Hu, *Natl. Sci. Rev.* **10**, nwac199 (2023).
- [9] H. Zhao, H. Li, B. R. Ortiz, S. M. Teicher, T. Park, M. Ye, Z. Wang, L. Balents, S. D. Wilson, and I. Zeljkovic, *Nature* **599**, 216 (2021).
- [10] Z. Guguchia, C. Mielke III, D. Das, R. Gupta, J. Yin, H. Liu, Q. Yin, M. Christensen, Z. Tu, C. Gong, and N. Shumiya, *Nat. Commun.* **14**, 153 (2023).
- [11] S. Chaudhary, Shama, J. Singh, A. Consiglio, D. Di Sante, R. Thomale, and Y. Singh, *Phys. Rev. B* **107**, 085103 (2023).
- [12] X. Gui and R. J. Cava, *Chem. Mater.* **34**, 2824 (2022).
- [13] C. Mielke, Y. Qin, J.-X. Yin, H. Nakamura, D. Das, K. Guo, R. Khasanov, J. Chang, Z. Q. Wang, S. Jia, S. Nakatsuji, A. Amato, H. Luetkens, G. Xu, M. Z. Hasan, and Z. Guguchia, *Phys. Rev. Mater.* **5**, 034803 (2021).
- [14] M. Kang, S. Fang, J. Yoo, B. R. Ortiz, Y. M. Oey, J. Choi, S. H. Ryu, J. Kim, C. Jozwiak, A. Bostwick, E. Rotenberg, E. Kaxiras, J. G. Checkelsky, S. D. Wilson, J.-H. Park, and R. Comin, *Nat Mater* **22**, 186 (2023).
- [15] K. Górnicka, M. J. Winiarski, D. I. Walicka, *et al.*, *Sci Rep* **13**, 16704 (2023).
- [16] P. K. Meena, M. Mandal, P. Manna, S. Srivastava, S. Sharma, P. Mishra, and R. P. Singh, *Supercond. Sci. Technol.* **37**, 075004 (2024).
- [17] M. Mandal, A. Kataria, C. Patra, D. Singh, P. K. Biswas, A. D. Hillier, T. Das, and R. P. Singh, *Phys. Rev. B* **105**, 094513 (2022).
- [18] R. P. Singh, A. D. Hillier, B. Mazidian, J. Quintanilla, J. F. Annett, D. M. Paul, G. Balakrishnan, and M. R. Lees, *Phys. Rev. Lett.* **112**, 107002 (2014).
- [19] D. Singh, J. A. T. Barker, A. Thamizhavel, D. M. Paul, A. D. Hillier, and R. P. Singh, *Phys. Rev. B* **96**, 180501 (2017).
- [20] D. Singh, S. K. P., J. A. T. Barker, D. M. Paul, A. D. Hillier, and R. P. Singh, *Phys. Rev. B* **97**, 100505 (2018).
- [21] T. Shang, G. M. Pang, C. Baines, W. B. Jiang, W. Xie, A. Wang, M. Medarde, E. Pomjakushina, M. Shi, J. Mesot, H. Q. Yuan, and T. Shiroka, *Phys. Rev. B* **97**, 020502 (2018).
- [22] D. Singh, K. P. Sajilesh, S. Marik, P. K. Biswas, A. D. Hillier, and R. P. Singh, *J. Phys. Condens. Matter* **32**, 015602 (2019).
- [23] D. Singh, J. A. T. Barker, A. Thamizhavel, A. D. Hillier, D. M. Paul, and R. P. Singh, *J. Phys. Condens. Matter* **30**, 075601 (2018).
- [24] D. Singh, S. K. P., S. Marik, A. D. Hillier, and R. P. Singh, *Phys. Rev. B* **99**, 014516 (2019).
- [25] T. Shang, M. Smidman, S. K. Ghosh, C. Baines, L. J. Chang, D. J. Gawryluk, J. A. T. Barker, R. P. Singh, D. M. Paul, G. Balakrishnan, E. Pomjakushina, M. Shi, M. Medarde, A. D. Hillier, H. Q. Yuan, J. Quintanilla, J. Mesot, and T. Shiroka, *Phys. Rev. Lett.* **121**, 257002 (2018).
- [26] J. P. Wakefield, M. Kang, P. M. Neves, D. Oh, S. Fang, R. McTigue, S. Y. F. Zhao, T. N. Lamichhane, A. Chen, S. Lee, S. Park, J.-H. Park, C. Jozwiak, A. Bostwick, E. Rotenberg, A. Rajapitamahuni, E. Vescovo, J. L. McChesney, D. Graf, J. C. Palmstrom, T. Suzuki, M. Li,

- R. Comin, and J. G. Checkelsky, *Nature* **623**, 301 (2023).
- [27] K. Momma and F. Izumi, *J. Appl. Crystallogr.* **44**, 1272 (2011).
- [28] J. Rodriguez-Carvajal, in *satellite meeting on powder diffraction of the XV congress of the IUCr*, Vol. 127 (Toulouse, France), 1990).
- [29] A. Giorgi and E. Szklarz, *J. Less-Common Met.* **22**, 246 (1970).
- [30] H. Suhl, B. T. Matthias, and L. R. Walker, *Phys. Rev. Lett.* **3**, 552 (1959).
- [31] H. Wiesmann, M. Gurvitch, H. Lutz, A. Ghosh, B. Schwarz, M. Strongin, P. B. Allen, and J. W. Halley, *Phys. Rev. Lett.* **38**, 782 (1977).
- [32] G. Grimvall, *The electron-phonon interaction in metals* (1981).
- [33] M. Tinkham, *Introduction to Superconductivity*, 2nd ed. (McGraw - Hill, New York, 1996).
- [34] W. L. McMillan, *Phys. Rev.* **167**, 331 (1968).
- [35] M. Mandal, C. Patra, A. Kataria, D. Singh, P. K. Biswas, J. S. Lord, A. D. Hillier, and R. P. Singh, *Phys. Rev. B* **104**, 054509 (2021).
- [36] M. Mandal, S. K. P., R. R. Chowdhury, D. Singh, P. K. Biswas, A. D. Hillier, and R. P. Singh, *Phys. Rev. B* **103**, 054501 (2021).
- [37] M. Isobe, M. Arai, and N. Shirakawa, *Phys. Rev. B* **93**, 054519 (2016).
- [38] N. Nakai, P. Miranović, M. Ichioka, and K. Machida, *Phys. Rev. B* **70**, 100503 (2004).
- [39] M. Isobe, M. Arai, and N. Shirakawa, *Phys. Rev. B* **93**, 054519 (2016).
- [40] H. Padamsee, J. E. Neighbor, and C. A. Shiffman, *J. Low Temp. Phys.* **12**, 387 (1973).
- [41] R. Khasanov, D. Eshchenko, D. Di Castro, A. Shengelaya, F. La Mattina, A. Maisuradze, C. Baines, H. Luetkens, J. Karpinski, S. M. Kazakov, *et al.*, *Phys. Rev. B* **72**, 104504 (2005).
- [42] R. Khasanov, K. Conder, E. Pomjakushina, A. Amato, C. Baines, Z. Bukowski, J. Karpinski, S. Katrych, H.-H. Klauss, H. Luetkens, *et al.*, *Physical Review B—Condensed Matter and Materials Physics* **78**, 220510 (2008).
- [43] E. H. Brandt, *J. Low Temp. Phys.* **73**, 355 (1988).
- [44] E. H. Brandt, *Phys. Rev. B* **68**, 054506 (2003).
- [45] R. S. Hayano, Y. J. Uemura, J. Imazato, N. Nishida, T. Yamazaki, and R. Kubo, *Phys. Rev. B* **20**, 850 (1979).
- [46] A. Maisuradze, W. Schnelle, R. Khasanov, R. Gumeniuk, M. Nicklas, H. Rosner, A. Leithe-Jasper, Y. Grin, A. Amato, and P. Thalmeier, *Phys. Rev. B* **82**, 024524 (2010).
- [47] A. D. Hillier, J. Quintanilla, B. Mazidian, J. F. Annett, and R. Cywinski, *Physical Review Letters* **109**, 097001 (2012).
- [48] J. A. T. Barker, D. Singh, A. Thamizhavel, A. D. Hillier, M. R. Lees, G. Balakrishnan, D. M. Paul, and R. P. Singh, *Phys. Rev. Lett.* **115**, 267001 (2015).
- [49] D. A. Mayoh, A. D. Hillier, G. Balakrishnan, and M. R. Lees, *Phys. Rev. B* **103**, 024507 (2021).
- [50] D. Singh, M. S. Scheurer, A. D. Hillier, D. T. Adroja, and R. P. Singh, *Phys. Rev. B* **102**, 134511 (2020).
- [51] L. Shu, W. Higemoto, Y. Aoki, A. D. Hillier, K. Ohishi, K. Ishida, R. Kadono, A. Koda, O. O. Bernal, D. E. MacLaughlin, Y. Tunashima, Y. Yonezawa, S. Sanada, D. Kikuchi, H. Sato, H. Sugawara, T. U. Ito, and M. B. Maple, *Phys. Rev. B* **83**, 100504 (2011).
- [52] J. Zhang, Z. F. Ding, K. Huang, C. Tan, A. D. Hillier, P. K. Biswas, D. E. MacLaughlin, and L. Shu, *Phys. Rev. B* **100**, 024508 (2019).
- [53] A. Kataria, J. A. T. Verezhak, O. Prakash, R. K. Kushwaha, A. Thamizhavel, S. Ramakrishnan, M. S. Scheurer, A. D. Hillier, and R. P. Singh, *Phys. Rev. B* **107**, L100506 (2023).
- [54] J. Zhang, D. E. MacLaughlin, A. D. Hillier, Z. F. Ding, K. Huang, M. B. Maple, and L. Shu, *Phys. Rev. B* **91**, 104523 (2015).
- [55] Arushi, D. Singh, A. D. Hillier, M. S. Scheurer, and R. P. Singh, *Phys. Rev. B* **103**, 174502 (2021).
- [56] A. Kataria, J. A. T. Verezhak, O. Prakash, R. K. Kushwaha, A. Thamizhavel, S. Ramakrishnan, M. S. Scheurer, A. D. Hillier, and R. P. Singh, *Phys. Rev. B* **108**, 214512 (2023).
- [57] D. Singh, S. K. P., J. A. T. Barker, D. M. Paul, A. D. Hillier, and R. P. Singh, *Phys. Rev. B* **97**, 100505 (2018).
- [58] T. Shang, G. M. Pang, C. Baines, W. B. Jiang, W. Xie, A. Wang, M. Medarde, E. Pomjakushina, M. Shi, J. Mesot, H. Q. Yuan, and T. Shiroka, *Phys. Rev. B* **97**, 020502 (2018).
- [59] Y. J. Uemura, V. J. Emery, A. R. Moodenbaugh, M. Suenaga, D. C. Johnston, A. J. Jacobson, J. T. Lewandowski, J. H. Brewer, R. F. Kiefl, S. R. Kreitzman, G. M. Luke, T. Riseman, C. E. Stronach, W. J. Kossler, J. R. Kempton, X. H. Yu, D. Opie, and H. E. Schone, *Phys. Rev. B* **38**, 909 (1988).
- [60] Y. J. Uemura, G. M. Luke, B. J. Sternlieb, J. H. Brewer, J. F. Carolan, W. N. Hardy, R. Kadono, J. R. Kempton, R. F. Kiefl, S. R. Kreitzman, P. Mulhern, T. M. Riseman, D. L. Williams, B. X. Yang, S. Uchida, H. Takagi, J. Gopalakrishnan, A. W. Sleight, M. A. Subramanian, C. L. Chien, M. Z. Cieplak, G. Xiao, V. Y. Lee, B. W. Statt, C. E. Stronach, W. J. Kossler, and X. H. Yu, *Phys. Rev. Lett.* **62**, 2317 (1989).
- [61] Y. J. Uemura, L. P. Le, G. M. Luke, B. J. Sternlieb, W. D. Wu, J. H. Brewer, T. M. Riseman, C. L. Seaman, M. B. Maple, M. Ishikawa, D. G. Hinks, J. D. Jorgensen, G. Saito, and H. Yamochi, *Phys. Rev. Lett.* **66**, 2665 (1991).
- [62] A. D. Hillier and R. Cywinski, *Appl. Magn. Reson.* **13**, 95 (1997).
- [63] S. K. P., D. Singh, A. D. Hillier, and R. P. Singh, *Phys. Rev. B* **102**, 094515 (2020).
- [64] K. Hashimoto, K. Cho, T. Shibauchi, S. Kasahara, Y. Mizukami, R. Katsumata, Y. Tsuruhara, T. Terashima, H. Ikeda, M. A. Tanatar, H. Kitano, N. Salovich, R. W. Giannetta, P. Walmsley, A. Carrington, R. Prozorov, and Y. Matsuda, *Science* **336**, 1554 (2012).
- [65] R. Khasanov, H. Luetkens, A. Amato, H. H. Klauss, Z. A. Ren, J. Yang, W. Lu, and Z. X. Zhao, *Phys. Rev. B* **78**, 092506 (2008).
- [66] J. A. T. Barker, B. D. Breen, R. Hanson, A. D. Hillier, M. R. Lees, G. Balakrishnan, D. M. Paul, and R. P. Singh, *Phys. Rev. B* **98**, 104506 (2018).
- [67] P. K. Biswas, M. R. Lees, A. D. Hillier, R. I. Smith, W. G. Marshall, and D. M. Paul, *Phys. Rev. B* **84**, 184529 (2011).